2017 IEEE International Conference on Robotics and Automation (ICRA)
Singapore, May 29 - June 3, 2017

Near-Surface Effects on the Controlled Motion of Magnetotactic Bacteria

Islam S. M. Khalil*, Ahmet Fatih Tabak†, Tijmen Hageman‡, Mohamed Ewis*,
Marc Pichel‡, Mohamed E. Mitwally*, Nermeen Serag El-Din*, Leon Abelmann‡§, and Metin Sitti†

***Abstract*— Magnetotactic bacteria have the potential to controllably reach stagnant fluids inside the human body and achieve targeted drug delivery. In this application, motion of the magnetotactic bacteria is influenced by the near-surface effects such as the background flows and surface interactions. Here, we provide a hydrodynamic model of bipolarly-flagellated magnetotactic bacteria (*Magnetospirillum gryphiswaldense* strain MSR-1) based on the resistive-force theory to resemble the helical body and the two flagella bundles, and investigate their swimming characteristics in two environments, i.e., free-space and near flat walls. The free-space is studied using capillary tubes with depth of 200 μm, whereas the effect of the flat walls is investigated using microfluidic chips with depth of 5 μm. We find that the linear speeds of bacteria near- and far-surface are 36$\pm$16.4 μm/s (mean$\pm$s.d.) and 46$\pm$6.8 μm/s, respectively, whereas their respective angular velocities are 12.5$\pm$5.7 rad/s and 13.5$\pm$5.0 rad/s.**

I. INTRODUCTION

Recently, there has been growing interest in the use of microorganisms to provide controlled locomotion at low Reynolds number [1]-[2]. This controlled locomotion is achieved in mainly two ways: Coupling motile microorganisms to a magnetic object and motion control of magnetic microorganisms. While the former method includes several complex fabrication steps [3], [4], surface treatment and bio-adhesion [6], and cell culturing, the latter method is relatively straightforward and relies only on cell culturing and magnetic steering using an external source of magnetic field. Directional control and maneuvering [7], [8], actuation of non-magnetic microobjects [9], [10], and micromanipulation and microassembly [11] have been demonstrated using magnetotactic bacteria under the influence of magnetic fields in milliTesla range. In addition to the mentioned nanotechnology applications, it is likely that the size ($\sim$5 μm in length and $\sim$500 nm in diameter) of the magnetotactic bacteria (Fig. 1) would enable them to reach deep-seated regions of the body via vessels using feedback of an imaging modality and external magnetic field for steering. Very recently, Felfoul *et al.* have utilized *Magnetococcus marinus* strain MC-1 to transport drug-loaded nanoliposomes into hypoxic regions of a tumour *in vivo* [12]. In this biomedical application of magnetotactic bacteria, the flagellated swim is influenced by the near-surface effects such as the background flows and surface interactions. Lauga *et al.* have shown that the hydrodynamic interactions of *Escherichia coli* with a boundary result in a hydrodynamic trapping (swimming in circular motion) of the cells close to the surface [13]. Lu and Martel have also investigated the wall effect on the swimming speed of *Magnetococcus marinus* strain MC-1 [9]. However, the hydrodynamics between the flagella bundles and the cell body, and the interactions between the rotating flagella bundle and the rotating helical body of the cell have not been modeled analytically. Here, we develop a hydrodynamic model of bipolarly-flagellated magnetotactic bacteria based on the resistive-force theory (RFT), to compare between the swimming characteristics (linear velocity, angular velocity, and radius of curvature) of magnetotactic bacteria close to and far from a surface. We also investigate the influence of the near-surface effects on the closed-loop control characteristics. The remainder of the

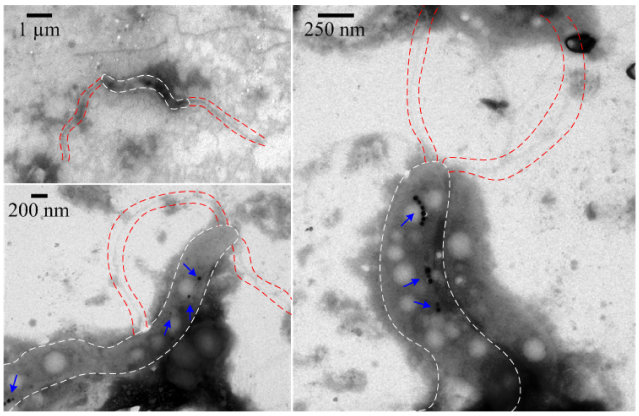

Fig. 1. Scanning and transmission electron microscopy images of bipolarly-flagellated magnetotactic bacteria (*Magnetospirillum gryphiswaldense* strain MSR-1). The white and red dashed lines indicate the cell of the bacterium and its flagella, respectively. Magnetotactic bacterium swims in a medium characterised by low Reynolds number using its two flagella bundles and the rotation of its helical body. The magnetite nanocrystals (blue arrows) that are enveloped in the cell of the bacterium enable directional control using earth's magnetic field. Here, we use external magnetic fields in milliTesla range to characterize and control the magnetotactic bacteria.

This work was supported by the DAAD-BMBF funding project and the Science and Technology Development Fund in Egypt (No. 23016).

*The authors are affiliated with the German University in Cairo, New Cairo City 11835, Egypt.

†The authors are affiliated with the Physical Intelligence Department, Max Planck Institute for Intelligent Systems, 70569 Stuttgart, Germany.

‡The authors are affiliated with the Korean Institute of Science and Technology, Saarbrücken 66111, Germany.

§L. Abelmann is affiliated with MESA+ Institute for Nanotechnology, University of Twente, 7500 AE Enschede, The Netherlands.

paper is organized as follows: Section II provides a hydrodynamic model of the magnetotactic bacteria that describes the helical propulsion, near- and far-surface effects, and the magnetic steering on the motion of the cells. Experimental results are presented in Seciton III using *Magnetospirillum gryphiswaldense* strain MSR-1 inside capillary tubes with depth of 200 μm and microfluidic chips with depth of 5 μm. Finally, Section IV concludes and provides directions for future work.

II. MODELING OF BIPOLARLLY-FLAGELLATED MAGNETOTACTIC BACTERIUM

We model the bipolarlly-flagellated magnetotactic bacterium as a helical body (with length l_{b}) with a magnetization vector oriented collinear to the helical axis. This assumption is not completely realistic due to cell-to-cell variability in the location and orientation of magnetite nanocrystals, as shown in Fig. 1. The flagella bundles (with length l_{f} and radius r_{f}) are also modeled as two helices attached to the ends of the helical body, as shown in Fig. 2. The growth medium gap between the bacterium and the surface has hight h. We also model the magnetic interaction between the dipole moment of the bacterium and external magnetic fields (electromagnetic system with 4 orthogonal coils is used [14]). The components of the electromagnetic fields, at the position (x, y, z) of the bacterium, are calculated based on [15] as follows:

$$B_x = \left(\frac{5}{4}\right)^{\frac{3}{2}} \frac{B_0}{4\pi} \int_0^{2\pi} \left(1 - \frac{y}{r}\cos\theta - \frac{z}{r}\sin\theta\right) F_0^{-\frac{3}{2}} \mathrm{d}\theta, \tag{1}$$

where B_x is the magnetic field along x-axis and r is the inner-radius of the electromagnetic coil. Moreover, B_0 is given by

$$B_0 = \left(\frac{4}{5}\right)^{\frac{3}{2}} \frac{\mu_0 N I_{\mathrm{c}}}{r}. \tag{2}$$

In (2), μ_0, N, and I_{c} are the permeability of the iron-core, number of turns of each coil, and the input current to each of the electromagnetic coils, respectively. Further, F_0 is given by

$$F_0 = \left(\frac{x}{r}\right)^2 + \left(\frac{y}{r} - \cos\theta\right)^2 + \left(\frac{z}{r} - \sin\theta\right)^2. \tag{3}$$

The magnetic field along y-axis (B_y) is calculated using

$$B_y = \left(\frac{5}{4}\right)^{\frac{3}{2}} \frac{B_0}{4\pi} \int_0^{2\pi} \left(\frac{x}{r}\frac{\cos\theta}{F_0^{\frac{3}{2}}}\right) \mathrm{d}\theta. \tag{4}$$

Finally, the magnetic field along z-axis (B_z) is given by

$$B_z = \left(\frac{5}{4}\right)^{\frac{3}{2}} \frac{B_0}{4\pi} \int_0^{2\pi} \left(\frac{x}{r}\frac{\sin\theta}{F_0^{\frac{3}{2}}}\right) \mathrm{d}\theta. \tag{5}$$

The magnetic field gradient is calculated numerically using (1), (4), and (5) to determine the magnetic force and torque exerted on the magnetic dipole of the bacterium. Once $\mathbf{B} = (B_x \;\; B_y \;\; B_z)^{\mathrm{T}}$ field is calculated, the magnetic force ($\mathbf{F}_{\mathrm{m}}$) and magnetic torque ($\mathbf{T}_{\mathrm{m}}$) vectors on an individual bacterium are calculated as:

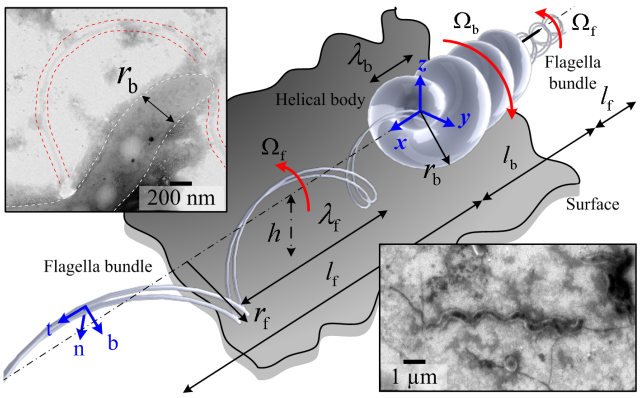

Fig. 2. A schematic representation of the helical propulsion of a magnetotactic bacterium with two helical flagella bundles at both ends of its helical body. Lengths of each bundle and the body are denoted with l_{f} and l_{b}, respectively. The helical body rotates with an angular velocity Ω_{b}, whereas the flagella bundles rotate in the opposite direction with an angular velocity Ω_{f}. λ_{b} and λ_{f} are the wavelengths of the body and bundles, respectively. The amplitude (outer radius) of the waves of the body and bundles are denoted with r_{b} and r_{f}, respectively. The bacterium has a local proximity h to a nearby surface. Local Frenet-Serret frame coordinates are indicated with surface tangent ($\mathbf{t}$), normal ($\mathbf{n}$) and binormal ($\mathbf{b}$), whereas x, y, and z indicate the bacterium frame of reference. The top-left inset shows a transmission electron microscopy image of a magnetotactic bacterium. The white and red dashed lines indicate the cell and the flagella, respectively. The bottom-right inset shows the spiral body of the bacterium.

$$\begin{pmatrix} \mathbf{F}_{\mathrm{m}} \\ \mathbf{T}_{\mathrm{m}} \end{pmatrix} = \begin{pmatrix} (\mathbf{m}\cdot\nabla)\,\mathbf{R}_{\mathrm{Lab}}\mathbf{B} \\ \mathbf{m}\times\mathbf{R}_{\mathrm{Lab}}\mathbf{B} \end{pmatrix}, \tag{6}$$

where $\mathbf{m}$ is the total magnetization vector of the magnetotactic bacterium, and $\mathbf{R}_{\mathrm{Lab}}$ is the rotation matrix from laboratory frame of reference to the frame of reference of the magnetotactic bacterium (calculated using quaternions [16]) to incorporate the overall orientation of each bacterium. Motion of the bacterium is governed by

$$\begin{pmatrix} \mathbf{F}_{\mathrm{m}} + \mathbf{F}_{\mathrm{d}} + \mathbf{F}_{\mathrm{p}} \\ \mathbf{T}_{\mathrm{m}} + \mathbf{T}_{\mathrm{d}} + \mathbf{T}_{\mathrm{p}} \end{pmatrix} = 0, \tag{7}$$

where $\mathbf{F}_{\mathrm{d}}$ and $\mathbf{T}_{\mathrm{d}}$ are the viscous drag force and torque vectors, respectively, and $\mathbf{F}_{\mathrm{p}}$ and $\mathbf{T}_{\mathrm{p}}$ denote the propulsive force and torque of the rotating helical flagella bundles, respectively, of an individual magnetotactic bacterium. The viscous drag on the bacterium is calculated based on RFT and the resultant viscous resistance matrices. The medium resistance ($\mathbf{B}_{\mathrm{f}_i}$) of the ith flagella bundle is calculated as follows [17]:

$$\mathbf{B}_{\mathrm{f}_i} = \int_0^{l_{\mathrm{f}_i}} \begin{pmatrix} \mathbf{R}_{\mathrm{f}_i}\mathbf{C}_{\mathrm{f}_i}\mathbf{R}_{\mathrm{f}_i}^{\mathrm{T}} & -\mathbf{R}_{\mathrm{f}_i}\mathbf{C}_{\mathrm{f}_i}\mathbf{R}_{\mathrm{f}_i}^{\mathrm{T}}\mathbf{S}_{\mathrm{f}_i} \\ \mathbf{S}_{\mathrm{f}_i}\mathbf{R}_{\mathrm{f}_i}\mathbf{C}_{\mathrm{f}_i}\mathbf{R}_{\mathrm{f}_i}^{\mathrm{T}} & -\mathbf{S}_{\mathrm{f}_i}\mathbf{R}_{\mathrm{f}_i}\mathbf{C}_{\mathrm{f}_i}\mathbf{R}_{\mathrm{f}_i}^{\mathrm{T}}\mathbf{S}_{\mathrm{f}_i} \end{pmatrix} \mathrm{d}l_{\mathrm{f}_i}, \tag{8}$$

where l_{f_i} is the length of the ith helical flagella bundle, for $i = 1, 2$. Further, $\mathbf{C}_{\mathrm{f}_i}$ and $\mathbf{R}_{\mathrm{f}_i}$ are the diagonal matrix of the local resistive-force coefficients, and the rotation matrix from local Frenet-Serret coordinate frames $(\mathbf{t}, \mathbf{n}, \mathbf{b})$ to the inertial frame of reference of the bacterium (x, y, z), respectively [18]. $\mathbf{S}_{\mathrm{f}_i}$ is the skew-symmetric matrix satisfying the cross-products. The resistance matrix of the body is computed by superimposing resistance matrix of a blunt

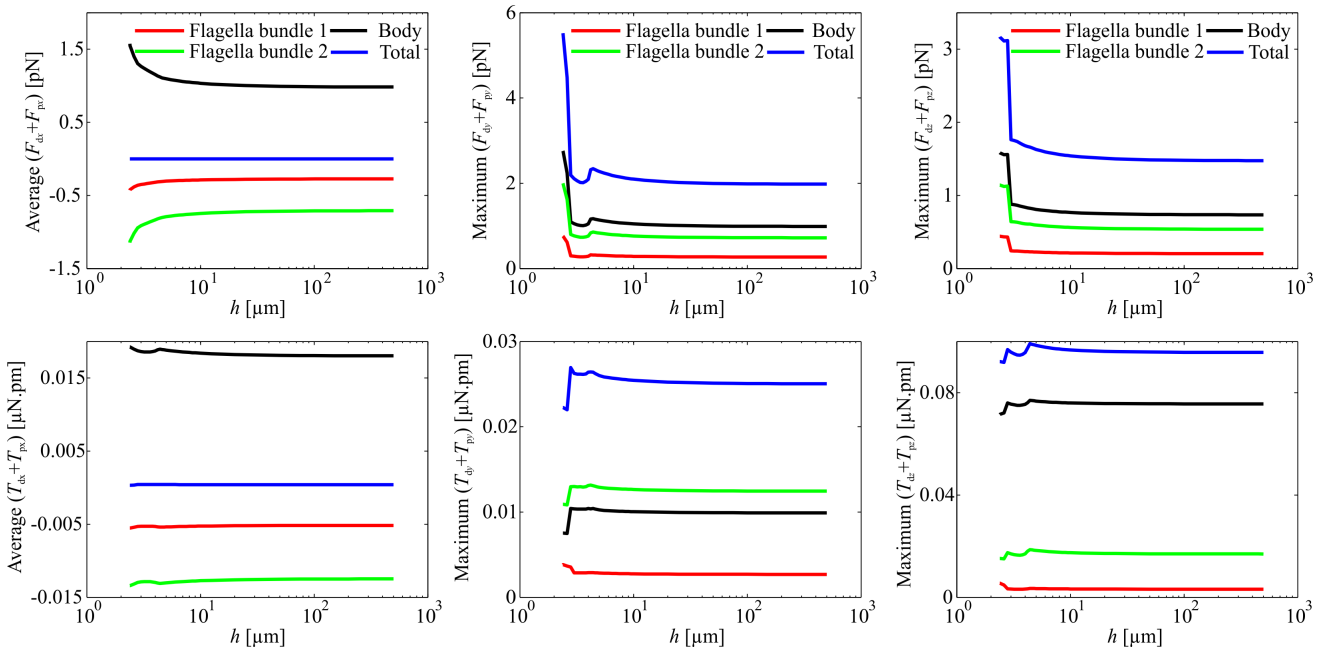

Fig. 3. Components of the drag and propulsive forces and torques on the body and flagella bundles of a magnetotactic bacterium are calculated using (16) and (17) against the distance between the helical body and the surface (h). The drag force components along x-, y-, and z-axis are represented using $F_{\mathrm{d}x}$, $F_{\mathrm{d}y}$, and $F_{\mathrm{d}z}$, respectively. The drag torque components with respect to x-, y-, and z-axis are represented using $T_{\mathrm{d}x}$, $T_{\mathrm{d}y}$, and $T_{\mathrm{d}z}$, respectively. $F_{\mathrm{p}x}$, $F_{\mathrm{p}y}$, and $F_{\mathrm{p}z}$ are the propulsive force components and $T_{\mathrm{p}x}$, $T_{\mathrm{p}y}$, and $T_{\mathrm{p}z}$ are the propulsive torque components along and with respect to x-, y-, and z-axis, respectively. The average and maximum values are calculated for the non-periodic and periodic force and torque components, respectively, along and with respect to x-, y-, and z-axis.

object and a helical geometry similar to (8), given that the resultant surface morphology of the body has a geometry of a screw. Therefore, the medium resistance ($\mathbf{B}_{\mathrm{b}}$) on the helical body is given by

$$\mathbf{B}_{\mathrm{b}} = \begin{pmatrix} \mathbf{D}_{\mathrm{b}} & -\mathbf{D}_{\mathrm{b}}\mathbf{S}_{\mathrm{b}} \\ \mathbf{S}_{\mathrm{b}}\mathbf{D}_{\mathrm{b}} & \mathbf{E}_{\mathrm{b}} \end{pmatrix} + \int_0^{l_{\mathrm{b}}} \begin{pmatrix} \mathbf{R}_{\mathrm{b}}\mathbf{C}_{\mathrm{b}}\mathbf{R}_{\mathrm{b}}^{\mathrm{T}} & -\mathbf{R}_{\mathrm{b}}\mathbf{C}_{\mathrm{b}}\mathbf{R}_{\mathrm{b}}^{\mathrm{T}}\mathbf{S}_{\mathrm{b}} \\ \mathbf{S}_{\mathrm{b}}\mathbf{R}_{\mathrm{b}}\mathbf{C}_{\mathrm{b}}\mathbf{R}_{\mathrm{b}}^{\mathrm{T}} & -\mathbf{S}_{\mathrm{b}}\mathbf{R}_{\mathrm{b}}\mathbf{C}_{\mathrm{b}}\mathbf{R}_{\mathrm{b}}^{\mathrm{T}}\mathbf{S}_{\mathrm{b}} \end{pmatrix} \mathrm{d}l_{\mathrm{b}}. \tag{9}$$

Matrices $\mathbf{C}_{\mathrm{b}}$, $\mathbf{D}_{\mathrm{b}}$, and $\mathbf{E}_{\mathrm{b}}$ contain the viscous resistance coefficients for the flagella bundle and body as follows:

$$\mathbf{C}_{\mathrm{b}} = -\begin{pmatrix} c_{\mathrm{t}} & 0 & 0 \\ 0 & c_{\mathrm{n}} & 0 \\ 0 & 0 & c_{\mathrm{b}} \end{pmatrix}, \tag{10}$$

where c_{t}, c_{n} and c_{b} are the local resistance coefficients along the Frenet-Serret frames of the helical flagella bundle and are articulated by Brennen and Winet [19]. The local resistance coefficient c_{t} is given by

$$c_{\mathrm{t}} = \left\{ \begin{array}{ll} \frac{2\pi\mu}{\log\left(\frac{2\lambda_j}{r_j}\right) - 0.807 - \frac{3\lambda_j}{8h}}, & \text{for } \frac{\lambda_j}{h} \leq 1 \\ \frac{2\pi\mu}{\log\left(\frac{2\lambda_j}{r_j}\right)}, & \text{for } \frac{\lambda_j}{h} > 1 \end{array} \right\}, \tag{11}$$

where μ is the dynamic viscosity of the growth medium and λ_j for $j = \mathrm{f}, \mathrm{b}$, is the wavelength of the bundle and body, respectively. Further, r_j for $j = \mathrm{f}, \mathrm{b}$, is the effective filament radius of the bundle and body, respectively. The local resistance coefficient c_{n} is calculated using

$$c_{\mathrm{n}} = \left\{ \begin{array}{ll} \frac{2\pi\mu}{\log\left(\frac{2\lambda_j}{r_j}\right) - 0.193 - \frac{3\lambda_j}{2h}}, & \text{for } \frac{\lambda_j}{h} \leq 1 \\ \frac{2\pi\mu}{\log\left(\frac{2\lambda_j}{r_j}\right) - 1}, & \text{for } \frac{\lambda_j}{h} > 1 \end{array} \right\}. \tag{12}$$

In (10), the local resistance coefficient c_{b} is given by

$$c_{\mathrm{b}} = \left\{ \begin{array}{ll} \frac{2\pi\mu}{\log\left(\frac{2\lambda}{r_j}\right) - 0.193 - \frac{3\lambda_j}{4h}}, & \text{for } \frac{\lambda_j}{h} \leq 1 \\ \frac{2\pi\mu}{\log\left(\frac{2\lambda}{r_j}\right)}, & \text{for } \frac{\lambda_j}{h} > 1 \end{array} \right\}. \tag{13}$$

In (9), $\mathbf{D}_{\mathrm{b}}$ is calculated as follows:

$$\mathbf{D}_{\mathrm{b}} = -6\zeta_{\mathrm{t}}\pi\mu \begin{pmatrix} 0.5 l_{\mathrm{b}} \log\left(\frac{r_{\mathrm{b}}}{h}\right) & 0 & 0 \\ 0 & \frac{r_{\mathrm{b}}^2}{h} & 0 \\ 0 & 0 & r_{\mathrm{b}} \log\left(\frac{r_{\mathrm{b}}}{h}\right) \end{pmatrix}, \tag{14}$$

where ζ_{t} is a translational tuning coefficient matrix to compensate for the effect of other geometric aberrations and surface roughness on translational drag. Further, l_{b} and r_{b} are the length and radius of the body of the magnetotactic bacterium, respectively. The z-axis is perpendicular to the surface, and hence as the proximity to this surface decreases, the lubrication effect increases with a logarithmic rate of change for motion along x- and z-axis. Therefore, the effect of proximity to the solid surface of the channel on body and flagella bundle is predicted by the formulae of drag coefficients and resistance force coefficients presented in [19] and [20]. Finally, for rigid-body translations of the magnetic

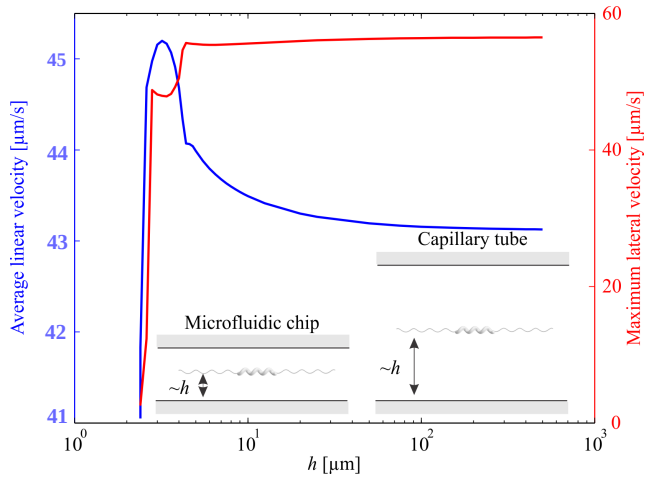

Fig. 4. Simulation results of the average linear and maximum lateral velocities of a magnetotactic bacterium. The linear velocity of a bacterium increases with the distance to the nearby surface (h). Maximum lateral velocity is calculated as the bacterium undergoes oscillatory motion along lateral directions with zero time average.

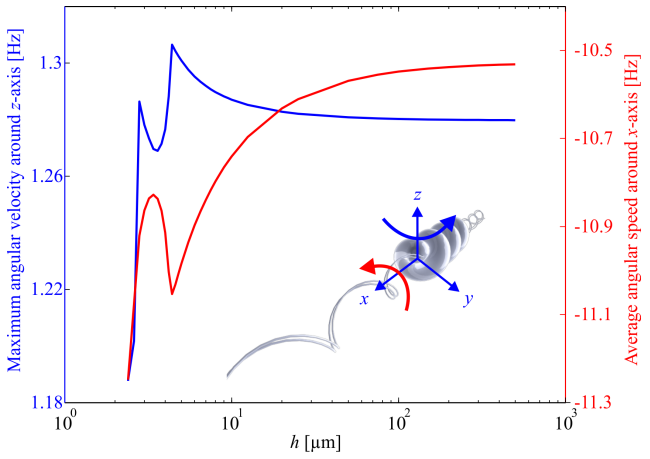

Fig. 5. Simulation results of the angular velocities with respect to x-axis and z-axis versus the distance to a nearby surface (h). Rotation around x-axis provides helical propulsion of the bacterium, whereas the rotation around z- or y-axis results in zig-zag trajectory of the bacterium. Maximum and average angular speeds are calculated because of the periodic and non-periodic patterns of the bacterium with respect to z- and x-axis, respectively. The negative values of the angular speed around x-axis are due to the conservation of angular momentum.

body we use:

$$\mathbf{E}_{\mathrm{b}} = -8\pi\mu\zeta_{\mathrm{r}} \begin{pmatrix} 0.5 l_{\mathrm{b}} r_{\mathrm{b}}^2 & 0 & 0 \\ 0 & 0.5 l_{\mathrm{b}} r_{\mathrm{b}}^2 & 0 \\ 0 & 0 & 0.5 l_{\mathrm{b}} r_{\mathrm{b}}^2 \end{pmatrix}, \qquad (15)$$

where ζ_{r} is a rotational tuning coefficient matrix. Using the resistance matrices given by (8) and (9), we calculate the drag force and torque vectors as follows:

$$\begin{pmatrix} \mathbf{F}_{\mathrm{d}} \\ \mathbf{T}_{\mathrm{d}} \end{pmatrix} = (\mathbf{B}_{\mathrm{f}_2} + \mathbf{B}_{\mathrm{f}_1} + \mathbf{B}_{\mathrm{b}}) \begin{pmatrix} \mathbf{U} \\ \Omega \end{pmatrix}, \qquad (16)$$

where $\mathbf{U}$ and Ω are the resultant linear and angular rigid-body velocities of the magnetotactic bacterium, respectively. The propulsion force and torque are given by

$$\begin{pmatrix} \mathbf{F}_{\mathrm{p}} \\ \mathbf{T}_{\mathrm{p}} \end{pmatrix} = \mathbf{B}_{\mathrm{f}_1} \begin{pmatrix} \mathbf{0} \\ \Omega_{\mathrm{f}_1} \end{pmatrix} + \mathbf{B}_{\mathrm{f}_2} \begin{pmatrix} \mathbf{0} \\ \Omega_{\mathrm{f}_2} \end{pmatrix}, \qquad (17)$$

where Ω_{f_i} denotes the rotation of the ith flagella bundle, i.e., $\Omega_{\mathrm{f}_i} = (0\ 0\ 2\pi f_i)^{\mathrm{T}}$ where f_i is the rotation frequency of the ith bundle. The helical body of the bacterium rotates in the opposite direction of the flagella to balance the torque of the bundles. We solve the equation of motion of the bacterium (7), and obtain its rigid body velocity vectors. In order to obtain the velocities and the position vector, in the laboratory frame of reference, we use:

$$\begin{pmatrix} \mathbf{U}_{\mathrm{Lab}} \\ \mathbf{\Omega}_{\mathrm{Lab}} \end{pmatrix} = \begin{pmatrix} \mathbf{R}_{\mathrm{Lab}} & \mathbf{0} \\ \mathbf{0} & \mathbb{I} \end{pmatrix}^{\mathrm{T}} \begin{pmatrix} \mathbf{U} \\ \mathbf{\Omega} \end{pmatrix}, \qquad (18)$$

where $\mathbb{I}$ is a 3×3 identity matrix. The effect of proximity to the solid surface of the channel on the body and the flagella bundle is predicted by the formula of drag coefficients and resistance force coefficients presented in [19] and [20]. The magnetotactic bacterium considered in this work is assumed to be neutrally buoyant. Also, it is observed that there is no tactile contact between the bacterium and the solid surface. Therefore, contact forces are not included in the model for simplicity.

We begin by solving (7) numerically. The helical flagella bundles and the helical body surface are discretized with 100 mesh nodes per complete wave for the integrators (8) and (9). Each period is discretized with time step on the order of $\mathcal{O}(10^{-2})$ seconds. First, we calculate the drag and propulsion forces and torques exerted on the flagella bundles and the helical body using (16) and (17), respectively. The simulation parameters are provided in Table I. Fig. 3 shows the components of the drag and propulsive forces and torques. The force and torque along and with respect to x-axis are non-periodic, whereas the force and torque along and with respect to y- and z-axis are periodic and their time average is zero. Therefore, we calculate the average and maximum values for the force and torque components of x-axis and lateral

TABLE I

CHARACTERISTICS OF MAGNETOTACTIC BACTERIA (*Magnetospirillum gryphiswaldense* STRAIN MSR-1). THE DIMENSIONS OF THE BACTERIA ARE CALCULATED USING TRANSMISSION ELECTRON MICROSCOPY IMAGES, WHEREAS THE MAGNETIC PROPERTIES (BOUNDARY FREQUENCY ω_{b} AND DIPOLE MOMENT $\mathbf{m}$) ARE CHARACTERIZED USING THE *U-turn* APPROACH [14].

Parameter	Value	Parameter	Value
l_{b} [μm]	4.79	$2r_{\mathrm{b}}$ [μm]	0.62
l_{f} [μm]	4.79	μ [mPa.s]	1
$2r_{\mathrm{f}}$ [nm]	10	λ [μm]	4.79
Ω_{b} [rad/s]	62.8	Ω_{f} [rad/s]	−471.2
ζ_{t}	$[420\ 50\ 50]^{\mathrm{T}}$	ζ_{r}	$[75\ 200\ 200]^{\mathrm{T}}$
ω_{b} [rad/s]	15.7	$\lvert\ \mathbf{m}\ \rvert$ [A.m^2]	$\sim 2.5\times10^{-15}$

axes (y- and z-axis), respectively. These simulation results indicate that there exist a significant difference between the drag force and torque on the bacterium with respect to its proximity to a surface. Therefore, the linear and angular velocities are expected to vary as the bacterium swims close to a surface. To study this observation, we solve the equation of motion (7) by forward Euler integration over time. Similar to the drag and propulsive forces and torques, the velocity components along the lateral directions (y and z) are periodic. Therefore, we calculate the average linear velocity of the bacterium along x-axis and the maximum lateral velocity as shown in Fig. 4. The linear speed of the bacterium increases (and decreases for h <10 μm) with the proximity to a surface and converges to an asymptote when the cell is far from the surface. Our simulation results also show the significance of the location of the bacterium to the surface. A slight difference in the hight (h) of the bacterium has relatively high impact on the average linear and maximum lateral velocities of a bacterium near-surface. The linear speed of the bacterium increases approximately by 5% when the distance to the nearby surface is increased from 2.5 μm to 100 μm. As we move away from the surface, the variation in average linear and maximum lateral velocities decreases till they converge to asymptotes, as shown in Fig. 4. The forward velocity is observed at the maximum ratio of propulsive drag of the flagella bundle to the resistive drag of the total bacterium.

The solution of (7) also provides the angular velocity of the helical body with respect to the helical axis (x-axis), z-axis, and y-axis, as shown in Fig. 5. The bacterium undergoes periodic pattern with respect to z-axis or y-axis (experimentally we observe that bacteria swim along zig-zag trajectories), and non-periodic pattern with respect to the helical axis. Therefore, we calculate the maximum and average angular velocities of the bacterium with respect the lateral direction and the helical axis, respectively. The calculated angular velocities include peaks due to the balance between the resistive and propulsive drag forces and torques in the equation of motion. The rotating flagella bundles generate greater thrust when the bacterium is close to the surface, which should be compensated by the resistive drag. Therefore, there exist an optimal point based on a ratio of body diameter to the bundle diameter.

III. SWIMMING CHARACTERISTICS IN FREE-SPACE AND NEAR-SURFACE

Magnetospirillum gryphiswaldense strain MSR-1 is used in this study to compare the influence of near- and far-surface effects on their motion characteristics. This strain is obtained from the German collection of microorganisms and cell cultures (DSM 6361, Deutsche Sammlung von Mikro-organismen und Zellkulturen, Brunswick, Germany). The strain is inoculated in magnetospirilum growth medium with an oxygen concentration of 1%. The cultures are then cultivated at 26°C for two to four days. The samples are harvested and selected for experiments based on their response to external magnetic fields. The samples are contained inside capillary tubes (VitroCom, VitroTubes 3520-050, Mountain Lakes, USA) with inner-width and depth of 2 mm and 200 μm, respectively, to study the far-surface effects. Microfluidic chips with inner-width of 200 μm and depth of 5 μm are used to study the influence of near-surface effects [21]. The capillary tube and the microfluidic chip are mounted in the common center of four electromagnetic coils. Each coil is independently supplied with current input and provides maximum magnetic field of 14 mT. Equations (1) and (4) are used to generate in-plane magnetic field to control the motion of the bacteria. The cells are observed using a microscopic unit (MF Series 176 Measuring Microscopes, Mitutoyo, Kawasaki, Japan). Videos are acquired using a camera (avA1000-120kc, Basler Area Scan Camera, Basler AG, Ahrensburg, Germany) and a 20× Mitutoyo phase objective. The position of a bacterium is determined from the acquired videos using our feature tracking algorithm [14], whereas the depth of the bacterium is approximately 100 μm and 2.5 μm for bacteria inside the capillary tubes and microfluidic chips, respectively. Inside capillary tubes, magnetotactic bacteria often undergo out-of-plane motion along z-axis. Therefore, we adjust the focus of the microscopic unit to observe bacteria in the middle of the tube only. Therefore, the proximity to surface is approximately 100 μm. However, the depth of the microfluidic chips is equal to the depth of focus of our microscopic unit. Therefore, we assume that the observed bacteria are approximately in the middle of the microfluidic chip.

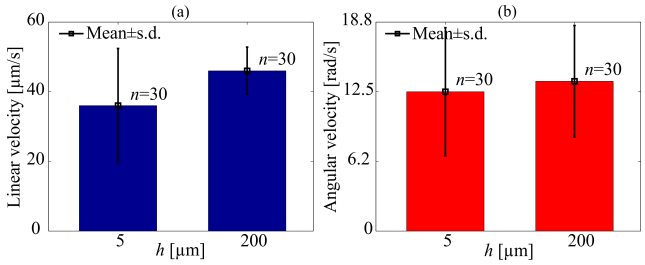

Fig. 6. Experimental results of the average linear and angular velocities of the magnetoelectric bacteria (*Magnetospirillum gryphiswaldense* strain MSR-1). (a) Linear velocity is calculated by applying uniform magnetic fields along single axis using two-opposite electromagnetic coils. The variability in measured linear velocity of the bacteria is more significant near-surface because of the logarithmic behaviour of the drag force and linear velocity of the bacterium. (b) Rotating magnetic fields are applied using two orthogonal coils supplied with synchronized sinusoidally varying current inputs. The mean and standard deviations (s.d.) are calculated using 30 different cells (n) from the same culture. The cells are observed approximately in the middle of the microfluidic chip ($h \approx 2.5$ μm) and capillary tube ($h \approx 100$ μm).

We begin by applying in-plane uniform magnetic fields and measure the linear speed of the magnetotactic bacteria in the capillary tubes and the microfluidic chips. The average linear speeds of bacteria from the same culture are shown in Fig. 6. The average speeds are calculated to be 36±16.4 μm/s (mean±s.d.) and 46±6.8 μm/s for near- and far-surface trials, respectively. The averages and standard deviations are calculated using 30 different cells (n=30) for the near- and far-surface experiments and the corresponding standard error

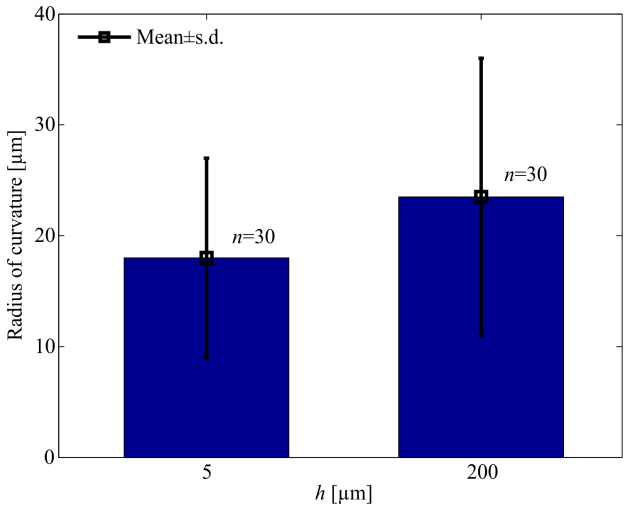

Fig. 7. Experimental results of the radius of curvature of the magnetoelectric bacteria (*Magnetospirillum gryphiswaldense* strain MSR-1). Rotating magnetic fields are applied using four electromagnetic coils and the radius of curvature is calculated using the circular trajectories taken by the bacteria. The mean and standard deviations (s.d.) are calculated using 30 different cells (n) from the same culture. The cells are observed approximately in the middle of the microfluidic chip ($h \approx 2.5$ μm) and capillary tube ($h \approx 100$ μm).

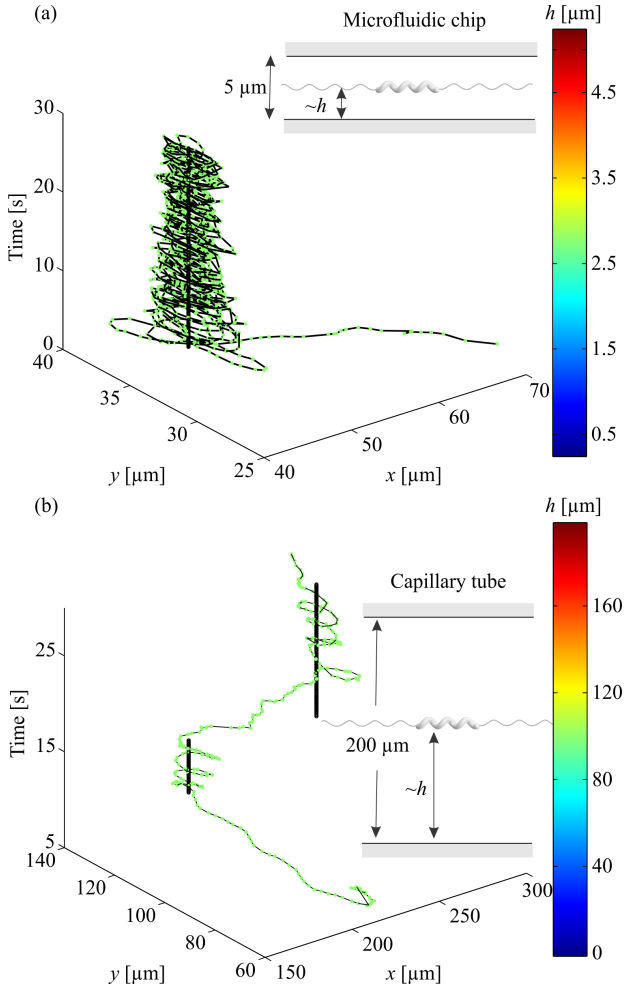

Fig. 8. Representative closed-loop control trials of magnetotactic bacteria (*Magnetospirillum gryphiswaldense* strain MSR-1). (a) Closed-loop control of a bacterium inside a microfluidic chip with depth (h) of 5 μm. (b) Closed-loop control of a bacterium inside a capillary tube with depth of 200 μm. The black trajectory and vertical black lines indicate the path taken by the controlled bacterium and the reference positions, respectively, whereas the green dots indicate the depth (bacteria are observed approximately in the middle of the tubes and chips) of the bacterium inside the capillary tube and the microfluidic chip. Bacteria close to surface are positioned with higher accuracy due to their restricted motion along z-axis.

of the mean (s.e.m.) are 2.9 μm/s and 1.2 μm/s, respectively. The drag force and torque on the magnetotactic bacteria is more significant when they swim near to a surface, as shown in the simulation results in Fig. 3. We apply a rotating magnetic field to study the influence of the rotational drag on the angular velocity of the bacteria. The rotating fields are generated by applying synchronized sinusoidally varying current inputs to the electromagnetic coils. The magnetic torque exerted on the magnetic dipole of each bacterium enables them to swim along circular trajectories. Fig. 6 shows the influence of the surface effect on the measured angular velocities of the bacteria. Angular velocities of 12.5±5.7 rad/s (s.e.m.=1.0 rad/s) and 13.5±5.0 rad/s (s.e.m.=0.9 rad/s) are measured for near- and far-surface, respectively. We also observe that bacteria near-surface undergo circular trajectories with smaller radius of curvature, as opposed to bacteria far from surface (Fig. 7). Under the influence of rotating magnetic fields, bacteria near a surface undergo circular trajectories with radius of curvature of 18.0±9 μm (s.e.m.=1.6 μm), whereas the radius of curvature of bacteria far from a surface is 23.5±12 μm (s.e.m.=2.1 μm). The difference between the means is larger than the standard deviation over 30 measurements. We attribute this observation to the cell-to-cell variability even within the same culture. Variability in the number of flagella, length of the body and length of flagella bundle, rate of rotation of the helical body and the flagella bundles, and number of magnetite nanocrystals within the body, is not included in our hydrodynamic model. Therefore, the hydrodynamic model predicts the effects of near-surface on identical cells, and show that there exist a significant influence of surface effect on identical cells. However, by assuming a Gaussian distribution, the standard errors are low and the difference between the means is statistically significant (in agreement with the theoretical model).

Figs. 3, 4, and 6 indicate the near-surface effects on the swimming speed, angular speed, and the radius of curvature of the magnetotactic bacteria. Therefore, we expect that a bacterium near a surface can be controlled with relatively higher positioning accuracy than a bacterium far from this surface. The influence of a closed-loop control system on the motion of magnetotactic bacteria is shown in Fig. 8. Closed-loop control is achieved by directing the magnetic field lines towards the reference position (vertical black lines) based on the position error of the bacterium with respect to the reference position [8]. Inside the microfluidic chips with depth of 5 μm, the controlled bacterium is observed approximately in the middle of the chip and its average speed is 24.7 μm/s, as shown in Fig. 8(a). The bacterium

undergoes circular trajectories within the vicinity of the reference position with a maximum radius of 10.6 μm. Fig. 8(b) shows the response of a controlled bacterium inside a capillary tube with depth of 200 μm. The bacterium is also controlled in-plane approximately in the middle of the tube. The average speed of the bacterium is 26.8 μm/s and the bacterium is trapped within the vicinity of two reference positions with maximum radii of 19.1 μm and 24.8 μm. It follows from the closed-loop control trials that the positioning accuracy of the bacteria increases for smaller distances between their body and a surface. The near-surface effect decreases the speed of the bacteria and this behaviour enables the control system to achieve positioning within relatively smaller regions. Near-surface effect also results in smaller radius of curvature and this behaviour also contributes to higher positioning accuracy.

IV. Conclusions and Future Work

We develop a hydrodynamic model of bipolarly-flagellated magnetotactic bacteria (*Magnetospirillum gryphiswaldense* strain MSR-1) to study the interactions between the flagella bundles and the helical body of the cell, and to investigate the influence of near-surface effects on the swimming characteristics. The results of this hydrodynamic model suggest that bacteria nearby a surface are subjected to greater drag force and drag torque than bacteria far from this surface. Our measurements show that the average linear and angular velocities of bacteria inside microfluidic chips with depth of 5 μm are 36$\pm$16.4 μm/s (n=30) and 12.5$\pm$5.7 rad/s (n=30), respectively, whereas the respective linear and angular velocities are 46$\pm$6.8 μm/s (n=30) and 13.5$\pm$5.0 rad/s (n=30) inside capillary tubes with depth of 200 μm. The experimental results do not show significant difference within the measurement error (difference between the means is larger than the standard deviation) due to the cell-to-cell variability. However, under the assumption of Gaussian distribution, the decrease in average speed between the far-surface and near-surface is statistically significant.

As part of future studies, the near-surface effects will be investigated using a group of microfluidic chips with several depths ranging from 5 μm to 200 μm. This range is devised based on our simulation results (Fig. 4 and Fig. 5 indicates multiple peaks that require experimental validation at each particular depth). Our electromagnetic system will also be adapted to provide feedback in three-dimensional space to measure the exact depth of the bacterium and analyse its influence on the motion characteristics. In addition, we will develop a scaled-up three-dimensional mockup of a bipolarly-flagellated magnetotactic bacterium to measure the drag forces and torques, and compare measurements to the theoretical results of the RTF-based hydrodynamic model.

References

[1] S. Martel, O. Felfoul, J.-B. Mathieu, A. Chanu, S. Tamaz, M. Mohammadi, M. Mankiewicz, and N. Tabatabaei, "MRI-based medical nanorobotic platform for the control of magnetic nanoparticles and flagellated bacteria for target interventions in human capillaries," *The International Journal of Robotics Research*, vol. 28, no. 9, pp. 1169-1182, September 2009.

[2] D. H. Kim, P. S. S. Kim, A. A. Julius, and M. J. Kim, "Three-dimensional control of engineered motile cellular microrobots," in *Proceedings of the IEEE International Conference on Robotics and Automation (ICRA)*, pp. 721-726, Minnesota, USA, May 2012.

[3] V. Magdanz, S. Sanchez, and O. G. Schmidt, "Development of a sperm-flagella driven micro-bio-robot", *Advanced Materials*, vol. 25, no. 45, pp. 6581–6588, September 2013.

[4] E. E. Hunter, N. Chodosh, E. B. Steager, and V. Kumar, "Control of microstructures propelled via bacterial baths," in *Proceedings of the IEEE International Conference on Robotics and Automation (ICRA)*, Stockholm, Sweden, pp. 1693-1700, May 2016.

[5] R. W. Carlsen, M. R. Edwards, J. Zhuang, C. Pacoret, and M. Sitti, "Magnetic steering control of multi-cellular bio-hybrid microswimmers," *Lab on a Chip*, vol. 14, no. 19, pp. 3850-3859, August 2014.

[6] B. Behkam and M. Sitti, "Bacterial flagella-based propulsion and on/off motion control of microscale objects", *Applied Physics Letters*, vol. 90 (023902), January 2007.

[7] I. S. M. Khalil and S. Misra, "Control characteristics of magnetotactic bacteria: *Magnetospirillum magnetotacticum* strain MS-1 and *Magnetospirillum magneticum* Strain AMB-1" *IEEE Transactions On Magnetics,* vol. 50, no. 4 (5000211), April 2014.

[8] I. S. M. Khalil, M. P. Pichel, L. Abelmann, and S. Misra, "Closed-loop control of magnetotactic bacteria," *The International Journal of Robotics Research*, vol. 32, no. 6, pp. 637-649, May 2013.

[9] Z. Lu and S. Martel, "Preliminary investigation of bio-carriers using magnetotactic bacteria," in *Proceedings of The IEEE Engineering in Medicine and Biology Society Annual International Conference (EMBS)*, pp. 683-686, New York City, USA, September 2006.

[10] Z. Lu and S. Martel, "Controlled bio-carriers based on magnetotactic bacteria," in *Proceedings of The IEEE International Conference on Solid-State Sensors, Actuators and Microsystems*, pp. 683-686, Lyon, France, June 2007.

[11] S. Martel and M. Mohammadi, "Using a swarm of self-propelled natural microrobots in the form of flagellated bacteria to perform complex micro-assembly tasks," in *Proceedings of The IEEE International Conference on Robotics and Automation (ICRA)*, pp. 500-505, Alaska, USA, May 2010.

[12] O. Felfoul, M. Mohammadi, S. Taherkhani, D. de Lanauze, Y. Z. Xu, D. Loghin, S. Essa, S. Jancik, D. Houle, M. Lafleur, L. Gaboury, M. Tabrizian, N. Kaou, M. Atkin, T. Vuong, G. Batist, N. Beauchemin, D. Radzioch, and S. Martel, "Magneto-aerotactic bacteria deliver drug-containing nanoliposomes to tumour hypoxic regions", *Nature Nanotechnology*, August 2016

[13] E. Lauga, W. R. DiLuzio, G. M. Whitesides, and H. A. Stone, "Swimming in circles: motion of bacteria near solid boundaries", *Biophysical Journal*, vol. 90, pp. 400-412, January 2006.

[14] H. A. Hassan, M. Pichel, T. Hageman, L. Abelmann, and I. S. M. Khalil, "Influence of the magnetic field on the two-dimensional control of *magnetospirillum gryphiswaldense* strain MSR-1," in *Proceedings of the IEEE/RSJ International Conference of Robotics and Systems (IROS)*, pp. 5119–5124, Daejeon, Korea, October 2016.

[15] R. Beiranvand, "Analyzing the uniformity of the generated magnetic field by a practical one dimensional Helmholtz coils system," *Review of Scientific Instruments*, vol. 84, pp. 075109 (1-11), 2013.

[16] J. Funda, R. H. Taylor, R. P. Paul, "On homogeneous transforms, quaternions, and computational efficiency," *IEEE Transactions on Robotics and Automation*, vol. 6, no. 3, pp. 382-388, June 1990.

[17] A. F. Tabak and S. Yesilyurt, "Improved kinematic models for two-link helical micro/nanoswimmers," *IEEE Transactions on Robotics*, vol. 30, no. 1, pp. 14-25, February 2014.

[18] A. J. Hanson and H. Ma, "Quaternion frame approach to streamline visualization," *IEEE Transactions on Visualization and Computer Graphics*, vol. 1, no. 2, pp. 164-174, June 1995.

[19] C. Brennen and H. Winet, "Fluid mechanics of propulsion by cilia and flagella," *Annual Review of Fluid Mechanics*, vol. 9, pp. 339-398, January 1977.

[20] J. J. L. Higdon and G. P. Muldowney, "Resistance functions for spherical particles, droplets, and bubbles in cylindrical tubes," *Journal of Fluid Mechanics*, vol. 298, pp. 192-210, September 1995.

[21] I. S. M. Khalil, M. P. Pichel, B. A. Reefman, O. S. Sukas, L. Abelmann, and S. Misra, "Control of magnetotactic bacterium in a microfabricated maze", in *Proceedings of the IEEE International Conference on Robotics and Automation (ICRA)*, Karlsruhe, Germany, pp. 5488–5493, May 2013.